Elemental Detection of Fluorochemicals by Nanospray-Induced Chemical Ionization in Afterglow of an Inductively Coupled Plasma

Samuel White, Kunyu Zheng,^a Jordan Tanen, Joseph E. Lesniewski,^β and Kaveh Jorabchi^{*}

Department of Chemistry, Georgetown University, Washington, D.C. 20057, United States

^{*} Corresponding author, kj256@georgetown.edu

^α Currently at AbbVie Inc., North Chicago, IL, 60064, United States

β Currently at Wilson Sonsini Goodrich & Rosati, Washington, D.C. 20006, United States

Abstract

Increased applications of fluorochemicals have prompted development of elemental methods for detection and quantitation of these compounds. However, high-sensitivity detection of fluorine is a challenge because of difficulties in excitation and ionization of this element. Recently, a new approach has emerged to detect F as a diatomic ion (BaF⁺) in inductively coupled plasma mass spectrometry (ICP-MS). However, formation of this species in the high-temperature plasma is inefficient, leading to low sensitivities. Here, we introduce a post-ICP chemical ionization approach to enhance analytical performance for F detection in liquid samples. Solutions of fluorochemicals are introduced into an ICP leading to formation of HF in the afterglow. Subsequently, reagent ions from nanospray of sodium acetate and barium acetate electrolytes are utilized to ionize HF to Na₂F⁺ and BaF⁺, respectively, via post-plasma ion-neutral reactions. Both ions provide substantially better sensitivities compared to that of BaF⁺ formed inside the plasma in conventional ICP-MS methods. Notably, post-plasma BaF⁺ offers a sensitivity of 280 cps/ppb for F, near two orders of magnitude higher than that of conventional ICP-MS methods. Compound-independent response for F from structurally diverse organofluorines is confirmed by monitoring BaF⁺ and a limit of detection (LOD) of 8-11 ng/mL F is achieved. Importantly, isobaric interferences are substantially reduced in chemical ionization, leaving F background as the main factor in LOD determination. Insights into BaF+ formation via experimental and computational investigations suggest that BaNO₂⁺ and Ba(H₂O)_n²⁺ serve as reagent ions while nonreactive BaCH₃CO₂⁺ is the dominant ion produced by nanospray. The facile development of effective post-plasma ionization chemistries using the presented approach offers a path for further improvements in F elemental analysis.

Introduction

Fluorochemicals have become popular among pharmacetuicals, ^{1,2} agrochemicals, ³ firefighting foams, ⁴ and flame retardant materials, ⁵ thanks to desirable physicochemical properties imparted in molecules upon fluorination. On the other hand, the improved stability of fluorochemicals (especially per- and polyfluorinated compounds) has led to increased environmental contaminations and challenges in wastewater treatment technologies to eliminate these compounds. ^{6,7} Notably, biological and environmental transformations of fluorochemicals also play critical roles in applications and fates of this class of compounds. For example, metabolites of newly developed drugs must be identified and quantified early in drug development to ensure safety and efficacy of pharmaceuticals. Similarly, new compounds may form upon wastewater treatment and environmental degradation of fluorochemicals, necessitating detection and safety assessment of such products. Accordingly, improved analytical techniques are needed for characterization of fluorochemicals and their transformation products at low concentrations in variety of matrices.

Among analytical methods, liquid chromatography-mass spectrometry (LC-MS) using soft ionization techniques such as electrospray ionization has served a key role in detection and identification of fluorochemicals, owing to excellent selectivity and sensitivity. 10,11 However, quantitation of analytes using soft ionization techniques requires compound-specific standards because of differences in ionization efficiencies between the analytes. 12,13 In many occasions, such standards are not readily available, creating major hurdles in quantitation. 8,13

Notably, elemental detectors can offer quantitation in the absence of standards. Elemental response factors are compound-independent and elemental methods often provide better matrix tolerance relative to molecular detection methods. As such, quantitation without compound-specific standards is attainable by elemental quantitation of LC-separated compounds and consideration of molecular formulas. This strategy has been successfully employed for S-, P-, and Cl-containing compounds. However, quantitation of

fluorochemicals using this approach has not advanced significantly because of challenges in highsensitivity elemental detection of F in LC eluates as discussed below.

Difficulties in atomic emission spectroscopy of F relate to inefficient excitation of this atom to high-energy states (>14.5 eV above ground sate)¹⁶ from which prominent UV-Vis emissions (non-VUV lines) occur. Plasma cooling upon solvent introduction further compromises the excitation efficiency and increases susceptibility to matrix effects, leading to challenges in liquid sample analysis. Recently, substantial improvements have been reported using electrothermal vaporization-inductively coupled plasma (ICP) atomic emission spectroscopy with internal standardization based on argon emission lines to account for plasma loading, providing detection limits of ~40 ng/g and 70 pg F in solutions.¹⁷ However, the discrete nature of sample introduction in this method does not lend itself to facile coupling to LC. Moreover, the drying and vaporization steps for solutions may create non-linearities, compromising analytical performance.¹⁸

To enhance optical detection capabilities, conversion of F to short-lived diatomic species in a high temperature environment has been attempted. In molecular absorption spectroscopy (MAS), fluorinated compounds are deposited in a furnace along with a metal salt and a modifier. A multi-step heating program is then applied to dry the sample followed by vaporization and atomization, leading to formation of diatomic metal-fluoride gas-phase species such as GaF^{19,20} and CaF.²¹ These species provide readily accessible molecular absorption bands in UV-Vis range. Moreover, the broader absorption profiles compared to elemental lines allow use of continuum photon sources for absorption measurements, further facilitating analytical measurements. A wide range of instrumental F detection limits (0.1 ng/mL¹⁹-100 ng/mL²¹ F, corresponding to 4-500 pg F) have been reported using this approach. While the low-pg detection in some studies offer a promising performance for this technique, the need for off-line analysis as well as potential compound-specific effects during heating steps^{20,21} limit the applications of MAS as a quantitative F detector for LC. Recently, molecular emission from CaF formed in a microwave induced plasma (MIP) was reported, enabling direct solution infusion with a potential for facile LC coupling.²² However, the

detection limit was significantly higher (1100 ng/mL F) than that of MAS, compromising the potential of MIP molecular emission spectroscopy for high-sensitivity F detection in liquid samples.

Elemental mass spectrometry of F has experienced similar difficulties to those in optical measurements. Analysis of liquid samples has largely been limited to ICP-MS where high gas-temperature of ICP facilitates solution introduction and coupling with LC. However, thermal ionization of F to F⁺ is inefficient even at high temperatures of the ICP, severely compromising the sensitivity and detection limits for F analyses.^{23,24} To address this shortcoming, formation of BaF⁺ in the ICP has been investigated via introduction of a barium salt into the plasma along with fluorochemicals.²⁵⁻²⁷ However, BaF⁺ formation inside the ICP requires a careful tuning of the plasma temperature to minimize competing reactions such as barium oxide formation and atomization of BaF⁺ while promoting ionization reactions (e.g. Ba²⁺ and F-formations).^{25,27,28} These competing processes lead to a compromised ion formation efficiency and a narrow optimum operating range for plasma temperature, reducing sensitivity and robustness.^{27,28} Moreover, extensive isobaric interferences are imposed by Ba¹⁸OH⁺, necessitating MS/MS techniques via reactions of ions with O₂ or NH₃ in the collision cell, in turn reducing the ion flux to the detector.

To enhance formation efficiency of F-containing polyatomic ions, we have recently reported a modified scheme based on plasma assisted reaction chemical ionization (PARCI) using an ICP.²⁹ In this approach, ion formation is shifted from inside the high-temperature ICP to a cool afterglow region where chemical ionization reactions rather than thermal ionization events are dominant. We have shown that Na₂F⁺ is generated in the ICP afterglow upon introducing a sodium salt into the plasma along with fluorinated compounds. Sensitivities ~180 cps/ppb F in aqueous solutions are achieved²⁹ using a single-quadrupole instrument without the need for MS/MS, while BaF⁺ formation with ICP- MS/MS is limited to sensitivities of 2-4 cps/ppb.²⁶ Such drastic enhancement in sensitivity is a consequence of facile Na⁺ formation by the plasma and ensuing efficient ion-neutral reactions in the cool (~600 K) afterglow compared to thermal ionization mechanisms dominant inside the ICP.

Despite the successful improvements in sensitivity using PARCI for aqueous samples, our recent experience has also shown some of the drawbacks of the approach described above. For example, we have

observed a significant loss in sensitivity of fluorine detection using Na₂F⁺ when fluorochemicals are introduced in acetonitrile solvent or upon addition of oxygen to the plasma (needed for carbon deposition prevention on MS interface). Major variations in plasma chemical composition (e.g. introduction of organic solvents and oxygen) lead to alterations of reagent ions produced by the plasma, affecting ion-neutral reactions in the afterglow and limiting the applicability of elemental F detection in LC using this methodology.

To minimize effects of plasma chemical composition on afterglow chemical ionization, we have recently devised a new approach where reagent ions are supplied by an independent ion source (e.g. nanospray) directly to the afterglow area while plasma is only utilized to produce F-specific neutrals. The success of this decoupled ionization approach for F analysis was recently demonstrated using a dielectric barrier discharge to create HF from GC-separated fluorinated compounds followed by chemical ionization of HF to Na₂F⁺ with reagent ions generated by nanospray of sodium acetate.³⁰

Here we report implementation of nanospray-induced chemical ionization in the afterglow of an ICP for elemental detection and quantitation of fluorinated compounds in liquid samples, enabling applications of this approach with a wide range of LC techniques. We examine the interactions of the nanospray ions with ICP products to gain insights into chemical ionization reactions. Moreover, we compare two chemical ionization schemes for F analysis enabled by sodium acetate and barium acetate as nanospray electrolytes. These investigations lead to significant improvements in sensitivity of elemental F detection in LC eluates using mass spectrometric techniques.

Experimental

Reagents and sample preparation. Sodium acetate trihydrate (ACS grade, Fisher Scientific, Fairlawn, NJ) and barium acetate (Puratronic grade, Sigma Aldrich, Milwaukee, WI) were dissolved in $18.2 \text{ M}\Omega$ water to prepare nanospray electrolytes. Test analytes fluconazole, flurazepam, fluphenazine, fluoxetine, flunitrazepam, flecainide, paroxetine maleate, haloperidol, midazolam, and fluvoxamine were purchased

from Sigma Aldrich (Milwaukee, WI) as certified reference materials with concentrations of 1 or 2 mg/mL in methanol. The working standards were prepared from these stock solutions via dilution in 50:50 water:acetonitrile.

ICP-nanospray-MS. Figure 1 shows the instrumental setup for the ICP nanospray-MS. Compounds were introduced by flow injections using a 20 μL injection loop at 50 μL/min 50:50 water:acetonitrile by an HPLC pump (1200 series, Agilent Technologies, Santa Clara, CA) into a nebulizer (HEN-90, Meinhard, Golden, CO) operated at a constant argon flow rate of 1.4 L/min. The aerosols passed through a Meinhard cyclonic spray chamber and were mixed with 10 mL/min O₂ gas using a tangential mixer (Meinhard, Golden, CO). The flow of oxygen was controlled by applying 50 psi to an electronically controlled valve (Porter EPC, Parker Hannifin Corp, Hatfield, PA) placed upstream of a 13-cm long 100-μm id fused silica capillary acting as a flow restrictor. The oxygen flow was calibrated using a soap bubble flow meter. The total aerosol gas flow emerging from the tangential mixer was directed to the plasma via a 2.0 mm injector. The ICP was sustained at 1300 W (14 L/min outer gas flow, 1.2 L/min auxiliary flow) using a stand-alone RF generator (Nexion 2000, PerkinElmer Inc., Waltham, MA) with the torch box exhaust flow rate adjusted to produce 4.0 m/s air flow velocity at the bottom intake of the torch box.

The plasma was coupled to a water-cooled nickel sampler (Spectron, Ventura, CA) with an orifice size of 3 or 4 mm placed 10 mm downstream of the load coil. A quartz tube (71 mm long, ¼ in o.d., 4 mm i.d. sealed to the plasma sampling interface downstream of the sampling orifice using a graphite ferrule) allowed cooling of the plasma afterglow prior to the ionization region. An image of the quartz tube and the ionization area downstream of the cooled aluminum plate of the ICP interface is depicted in Figure S1 to complement the schematic in Figure 1. Note that the pressure in the quartz tube is close to atmospheric pressure unlike conventional ICP-MS where plasma sampling is accomplished by direct plasma gas expansion into the first vacuum stage of the MS. To increase plasma sampling into the quartz tube, a venturi device was constructed using a bored-through ¼" Swagelok tee and was attached to the end of the quartz tube using a graphite ferrule. The position of the venturi tee relative to the end of the quartz tube was optimized off line with the quartz tube and tee assembly on the bench. 5 L/min nitrogen was supplied to the

side arm of the tee using a mass flow controller (MKS instruments, Andover, MA) and the tee was slid along the quartz tube while aerodynamic sampling of the lab air at the upstream end of the tube was monitored using a mass flow meter (MKS instruments, Andover, MA). The position of the tee was marked when the maximal air sampling was achieved, denoting optimal venturi effect. The quartz tube and the tee were then transferred to the ICP interface without changing the tee positioning along the quartz tube.

Chemical ionization of plasma products sampled by the venturi device was achieved by supplying reagent ions generated from a borosilicate nanospray emitter (World Precision Instruments, Sarasota, FL, 0.75 mm i.d., 1 mm o.d.) pulled to \sim 5 µm tip size using a capillary puller (PN-3, Narishige Scientific Instrument Lab, Tokyo, Japan). The emitter was placed laterally \sim 1 cm away from the Swagelok tee end and at 45° angle. Axially, the emitter was \sim 5 mm downstream of the venturi tee end. A potential of 1600 V was applied to the nanospray electrolyte using a platinum wire and potentials of 400 V and 300 V were applied to the venturi tee and the MS curtain plate, respectively. These parameters created suitable electric fields to supply ions from the nanospray to the ionization area (between the venturi tee end and the MS plate) and to guide the ion-neutral reaction products to the MS. The exact voltage of the nanospray was optimized for each experiment to establish a stable spray. The nitrogen gas flow rate supplied to the venturi tee was optimized at values 2-2.6 L/min via maximizing analyte ion (Na₂F⁺ and BaF⁺) intensity upon flow injections of 20 μ M fluconazole as the test fluorinated compound. This procedure also resulted in the highest signal-to-background values.

Ion detection was performed by a triple quadrupole MS (API 3000, Sciex, Framingham, MA) operated in Q1 single-quadrupole mode. All analytical figure of merit (linearity, LOD, sensitivity) were characterized by monitoring analytical ions with 500 ms dwell time per ion. A N₂ counter flow gas (setting of 9 in Analyst software) introduced between the curtain plate and the MS sampling orifice restricted neutrals from entering the MS. Unless specified, the sampling orifice of the MS was biased to 50 V and the focusing ring potential was set to 100 V while skimmer was grounded and the Q0 was operated at -10 V bias. These ion sampling settings provided ion collisional activation for declustering of the ions.

To investigate reagent ions, MS scans were collected in 20-500 m/z range over 2 seconds/spectrum with 0.1 m/z steps. An average spectrum over 30 seconds was used for data analysis. In conditions where ion flux exceeded the detector linear range (> 2 x 10⁶ cps) in the scan mode, the ion flux was reduced by detuning the lens between Q2 and Q3. A lens potential of -22 V was used for normal operation while the potential was adjusted to -19 V in detuned mode. A factor of 15 reduction in ion flux was achieved in detuned mode, characterized based on comparison of m/z 157 baseline intensity (corresponding to BaF⁺) in normal and detuned modes.

Computational investigations. The Gaussian 16 software package³¹ was used to calculate the electronic energies at the ω B97xD/aug-cc-pVTZ level of theory with an ECP46MDF pseudopotential for barium. Thermochemistry of ion-neutral reactions were calculated at 298 K using the standard rigid rotor harmonic oscillator (RRHO) approximation. Low vibrational frequencies and internal rotations may introduce errors in thermochemical values using this approximation. Such errors are insignificant in evaluating energetic favorability of ionization reactions considered in this report given the sizable magnitude of the zero-point corrected reaction energies (Δ H_{0K}). Note that temperatures of 30-40 °C were recorded at the outlet of the venturi tee at optimized nitrogen flow rates. This observation indicates significant cooling of the plasma flow during the journey in the quartz tube and via mixing with the nitrogen in the venturi device, justifying the 298 K temperature selected for thermochemical calculations.

Results and Discussion

Post-ICP Na₂F⁺ formation. Our recent studies³⁰ have shown that HF produced by decomposition of fluorinated compounds in a solvent-free helium DBD can be ionized via:

 $HF_{(g)} + Na(CH_3CO_2Na)_{n^+(g)} \rightarrow Na(NaF)(CH_3CO_2Na)_{n-1^+(g)} + CH_3CO_2H_{(g)}$ Equation 1

where $Na(NaCH_3CO_2)_n^+$ reagent ions are produced by nanospray of sodium acetate electrolyte. To explore the applicability of these reagent ions for F detection in afterglow of an ICP loaded with 1:1 water: acetonitrile solvent and oxygen, we investigated the interactions of ions produced by nanospray of 1

mM sodium acetate with ICP afterglow. The detected ions from such interactions are depicted in Figure 2. $Na(NaCH_3CO_2)_n^+$ ions with n=1-5 produced by nanospray are prominent in the spectrum even after the interaction with the ICP afterglow, suggesting the viability of Equation 1 for F detection in ICP afterglow. Interestingly, $Na(NaNO_2)_m(NaCH_3CO_2)_n^+$ clusters are also detected. These ions are attributed to reactions of $Na(NaCH_3CO_2)_n^+$ with HNO_2 produced by the plasma loaded with solvent and oxygen.

Figure 3 depicts detection of Na₂F⁺ upon flow injections of a fluorinated compound, confirming successful conversion of organic F to HF via ICP-assisted reactions followed by chemical ionization with Na(CH₃CO₂Na)_n⁺ reagent ions. The successful formation of Na₂F⁺ from a plasma loaded with acetonitrile, water, and oxygen indicates enhanced robustness of ionization to plasma chemical environment compared to the previous approach where sodium was introduced into the ICP for afterglow reagent ion generation.²⁹ Further improvements in chemical ionization may be achieved by optimizing the concentration of reagent ions in the ionization area. To this end, Figure 4A depicts the effect of sodium acetate nanospray electrolyte concentration on Na₂F⁺ detection sensitivities (ion intensity detected per ppb of F) upon flow injections of 20 μM F (in the form of fluconazole) into the ICP. Sensitivity is improved from 14 to 45 cps/ppb with increasing electrolyte concentration. A similar enhancement is observed for reagent ion intensities in Figure 4B, indicating that higher electrolyte concentrations give rise to larger Na(NaCH₃CO₂)_n⁺ gas-phase concentrations, leading to higher ionization rates and more reaction products during the ionization time. Notably, the sensitivity at 10 mM is an order of magnitude higher than 2-4 cps/ppb offered by ICP-MS/MS.^{25,27,28} However, both the sensitivity and reagent ion intensities reach a plateau at higher electrolyte concentrations, denoting a limit for chemical ionization via Equation 1.

The plateauing of Na₂F⁺ signal and reagent ion intensities at higher concentrations of sodium acetate electrolyte are attributed to clustering. Chemical ionization of HF in Equation 1 requires a reagent ion to transfer two Na⁺ ions to counteract the negative charge from deprotonation of HF. Generating sufficient quantities of a reagent ion with two Na⁺ ions mandates high concentrations of sodium acetate in the nanospray electrolyte, leading to clustering of both reagent ion and the analytical ion. Extensive clustering of reagent ions is evident in Figure 2 at 1 mM sodium acetate electrolyte concentration. Clustering of the

analytical ion is shown in Figure 5 where prominent amounts of $Na_2F(NaCH_3CO_2)_2^+$ are observed at electrolyte concentrations of 1 mM and higher in addition to Na_2F^+ upon flow injections of a fluorinated compound.

Clustering distributes nanospray current among multiple reagent ions, reducing the concentration of each species, and in turn hampering efficient ionization of HF by each cluster ion. As a result, analytical signal is distributed among multiple m/z values, reducing the ion intensity at each m/z. A delustering potential of 50 V is used in our experiments at the MS ion sampling interface to fragment Na₂F⁺(NaCH₃CO₂)_n⁺ clusters into Na₂F⁺ in an attempt to improve the sensitivity using Na₂F⁺. However, extensive clustering still persists as shown in Figures 2 and 5. Moreover, efficiency of Na₂F⁺(NaCH₃CO₂)_n⁺ fragmentation to Na₂F⁺ is reduced as n increases. To enhance the analytical performance of F detection via post-plasma chemical ionization we investigated reagent ions with minimal clustering tendencies as discussed below.

Enhanced post-ICP chemical ionization using barium-based reagent ions. Cations with higher charge states can replace the two positive ions needed in HF ionization, thus allowing use of lower electrolyte concentrations for reagent ion generation. Further, electrostatic repulsion between multiply charged cations minimizes clustering in electrospray ion formation. We selected barium to test the efficacy of doubly charged ions for HF ionization because high affinity of this metal to F has recently been reported via formation of BaF $^+$ inside the high temperatures of an ICP. 26,32,33 However, in contrast to the conventional approach in ICP-MS/MS where ICP properties are finely tuned to form BaF $^+$ within the plasma, our approach introduces barium ions directly to the plasma afterglow for reaction with HF (see Figure 1). The sensitivities for F detection via BaF $^+$ formation in ICP-nanospray-MS are depicted in Figure 6A as a function of barium acetate electrolyte concentration upon flow injections of 20 μ M F into the ICP. Comparison of Figure 6A to 4A reveals two major differences between BaF $^+$ and Na $_2$ F $^+$ for F detection: 1) unlike Na $_2$ F $^+$, F detection efficiency using BaF $^+$ is independent of the electrolyte concentration in the range of 0.1-10 mM, and 2) BaF $^+$ offers drastically higher F detection sensitivity compared to Na $_2$ F $^+$ at all electrolyte concentrations. These results highlight the advantages of barium-based reagent ions for elemental F detection via post-plasma chemical ionization.

Insights into ionization mechanism. To gain insights into the underlying processes in barium-based ionization, we examined the ions detected from interactions of barium acetate nanospray with post-plasma flow. Figure 7A shows the detected ions using 1 mM barium acetate as nanospray electrolyte. Notably, the extent of clustering is minimal in Figure 7A compared to that observed in Figure 2, consistent with the hypothesis formulated above for multiply charged ions in electrospray.

Prominent ions in Figure 7A include BaCH₃CO₂⁺ and Ba²⁺ expected from nanospray as well as BaNO₂⁺, BaHCO₂⁺, BaNO₃⁺, BaHCO₃⁺ that result from interactions of initial nanospray ions with plasma products HCO₂H, HNO₂, HNO₃, and CO₂. These plasma products originate from introduction of solvents and oxygen into the plasma. Air diffusion into the plasma also contributes to formation of HNO₂ and HNO₃. BaOH⁺ and an unidentified peak at m/z 168 are also observed in Figure 7A but we hypothesized that these ions are largely products of fragmentation upon ion activation during ion sampling. To investigate this hypothesis, we utilized softer ion sampling parameters by lowering the declustering potential of the MS from 50 V to 10 V.

The soft ion sampling spectrum is depicted in Figure 7B where solvation (mainly hydration) of ions is evident, confirming significantly reduced ion activation. A more detailed annotation of the spectrum in Figure 7B is provided in Figure S2 while ion intensities are tabulated in Table S1. Importantly, aggregate intensities of fully desolvated species in Figure 7A (core ions) can be inferred from summation of intensities for each core ion and its associated solvated ions in the soft sampling spectrum of Figure 7B. These aggregate intensities are tabulated in Table S2. Ratios of aggregate intensities in soft and harsh ion sampling conditions in Table S2 indicate that prevalence of BaOH⁺ and m/z 168 increases by 2.3 and 4.4 folds, respectively, when harsher ion sampling is used while the prevalence of the other core ions is unaffected or decreased. This observation confirms the hypothesis that BaOH⁺ and m/z 168 largely originate from ion activation and fragmentation processes during ion sampling.

To assess the potential of the background ions for serving as reagent ions in BaF⁺ formation, we utilized computational investigations. Ion solvation may play a significant role in chemical ionization,³⁴ thus we used the soft ion sampling condition to gain insights into solvation extent of potential reagent ions. For

singly charged ions, prominent intensities of the core (fully desolvated) ions were detected in soft ion sampling conditions (Figure 7B and S2). Therefore, we considered only the fully desolvated species in our computational studies of singly charged ions to simplify the calculations.

Table 1 details the thermochemistries of reactions between HF and the major singly charged ions observed in the background spectra. The accuracy of these values may be estimated by comparison to experimental data. The thermochemistry of BaOH $^+$ reaction with HF is available from the experimental heats of formation of the species, 35 leading to an experimental $\Delta H_{298K} = -14.3 \pm 44.3$ kJ/mol compared to the computed value of -43.1 kJ/mol in Table 1. Unfortunately, the large experimental uncertainties render verification of computations challenging. Thus, the values in Table 1 are interpreted qualitatively to guide the understanding of ionization reactions.

The results in Table 1 suggest that BaNO₂⁺, BaOH⁺, BaHCO₃⁺ may serve as reagent ions for HF ionization while BaCH₃CO₂⁺, BaHCO₂⁺, and BaNO₃⁺ are unlikely to offer efficient ionization of HF. We note that BaOH⁺ may not be present in the ionization region (prior to ion sampling) in large quantities as discussed above. Further, reaction of BaHCO₃⁺ with HF is predicted to be spontaneous only if entropic contributions from dissociation of carbonic acid to H₂O and CO₂ are considered. This dissociation enhances the gas-phase basicity of HCO₃⁻, ³⁶ however, more detailed experimental and theoretical investigations are needed to ascertain similar effects for reactions of BaHCO₃⁺. Overall, BaNO₂⁺ appears the most promising reagent ion among the singly charged species because of its prevalence and its potentially favorable reaction suggested by the computations.

Figures 7B and S2 also show solvated Ba²⁺ species with solvation shells of 1-5 solvent molecules. To evaluate potential of doubly charged species as reagent ions, we calculated thermochemistry of Ba(H₂O)₃²⁺ reaction with HF as a representative, indicating an extremely favorable reaction as shown in Table 2. The resulting solvated BaF⁺ is desolvated during transfer to the MS and within the ion sampling process. Thus, solvated Ba²⁺ ions may be effective reagent ions for BaF⁺ formation. One must, however, note that kinetic barriers could reduce the effectiveness of reagent ions. Such barriers may be significant for ion-neutral reactions of doubly charged ions where a charge separation process leads to formation of singly charged

products, requiring extensive experimental and theoretical investigations to map the reaction pathway energetics.³⁷

Further mechanistic insights may be gleaned by examining the effect of electrolyte concentration on the background ions as illustrated in Figure 6B. BaCH₃CO₂⁺ intensity increases significantly with electrolyte concentration, while other major ions are generally unaffected. This observation along with unaffected BaF⁺ sensitivity in Figure 6A suggest that BaCH₃CO₂⁺ is not an effective reagent ion, in agreement with computational predictions

It is impressive that barium acetate electrolyte provides a dramatically improved ionization compared to sodium acetate electrolyte (Figure 6A vs Figure 4A), even though many of the prevalent species in barium acetate nanospray (e.g. BaCH₃CO₂⁺ and BaHCO₂⁺ in Figure 7A) are poor reagent ions. However, a comparison of Figure 2 to Figure 7A reveals that the potentially effective reagent ions, namely BaNO₂⁺ and Ba²⁺ (resulting from declustering of solvated Ba²⁺), have over 10-fold higher intensities compared to Na(CH₃CO₂Na)_n⁺ reagent ions produced by sodium acetate electrolyte. Thus, the improved ionization using barium acetate electrolyte is attributed to enhanced reagent ion concentrations. Tuning the electrolyte properties to focus the nanospray current into effective reagent ions would further improve the sensitivity of ionization in ICP-nanospray MS.

Considering the significant enhancement of ionization by barium acetate electrolyte, the remainder of this report is focused on exploring the analytical potential of the barium-based chemical ionization approach in the afterglow of an ICP. A barium acetate electrolyte concentration of 1 mM was used for all ensuing experiments.

Compound-independent F detection. As noted above, compound-independent elemental responses constitute a major advantage of elemental methods compared to molecular ionization in LC-MS for quantitation. To evaluate this capability in ICP-nanospray-MS, we tested a number of fluorinated compounds via flow injections. Table 2 compares the F response factors defined as flow injection peak areas per mol of F observed for various compounds. For ease of comparisons, the response factors are normalized to the average response factor from all compounds. Note that a normalized response factor of

unity represents an ideal behavior. The results in Table 2 indicate close to ideal behavior and suggest that conversion of F in analytes to HF via plasma assisted reactions occurs in a quantitative manner, ensuring elemental quantitation capabilities.

Analytical performance and comparison to ICP-MS. The linearity of response in ICP-nanospray-MS is indicated in Figure 8 via a calibration curve constructed from flow injection peak areas in the concentration range of blank-101 μM F (0-1919 ng/mL F in the form of fluconazole). An LOD of 8 ng/mL F is estimated based on $3\sigma_{blank}$ /slope where σ_{blank} is the standard deviation of the peak area for 6 blank flow injections. Constructing a calibration curve based on peak heights yields a sensitivity of 281 cps/ppb F while a detection limit of 11 ng/mL F is estimated from $\sigma_{baseline}$ /sensitivity where $\sigma_{baseline}$ is the standard deviation of BaF⁺ baseline intensity measured for 30 seconds with 500 ms dwell time when only solvent is infused. Table 3 compares the analytical performance of ICP-nanospray-MS to other recent ICP-MS methods for F detection. All of the methods in Table 3 utilize the same analytical ion, BaF⁺. However, this ion is formed via chemical ionization in the afterglow for ICP-nanospray-MS while thermal ionization inside the ICP creates BaF+in all other ICP-MS methods. Evidently, ICP-nanospray-MS offers drastically higher sensitivities (70 to 700-fold) compared to other ICP-MS techniques. This is partly related to lower isobaric interferences in chemical ionization. In ICP-MS methods, Ba¹⁸OH⁺ exerts a major isobaric interference for detection of BaF⁺ to the extent that BaF⁺ signal from 2500 ng/mL F injection is undetected without MS/MS reactions to remove the interference.²⁷ Unfortunately, MS/MS reactions also reduce the ion flux of BaF⁺ to the detector, resulting in reduced sensitivities. Ba¹⁸OH⁺ interference may also be reduced by limiting the solvent load into the plasma via argon dilution of the aerosol gas. 32 However, severe loss of sensitivity (0.4 cps/ppb F) accompanies this approach as the analyte introduction into the plasma also suffers.

Importantly, reduced sensitivities in conventional ICP-MS methods lead to compromised precision for F detection. This effect is shown in Table 3 where contribution of counting statistics to net signal reproducibility is compared among various methods for a 100 ng/mL F sample measured with a 500-ms dwell time. The actual experimental precision will have additional contributions such as those from plasma instabilities. It is clear from Table 3 that low sensitivity in conventional ICP-MS leads to major contribution

of counting variation to imprecision. This limitation is exacerbated when fast chromatographic separations are used, requiring even shorter dwell times to capture the transient peaks. In contrast, the high sensitivity in ICP-nanospray-MS drastically reduces the effects of counting variation. In our measurements, baseline intensity at m/z 157 is routinely measured with RSD <4 % using a 500 ms dwell time, quantifying contributions of all noise sources including plasma and nanospray instabilities and mixing dynamics in the afterglow. A reproducibility of 4% RSD for both signal and baseline intensities amounts to 14% RSD for the net signal in ICP-nanospray-MS of a 100 ng/mL F solution measured using 500 ms dwell time. We note that the precision can be further improved by modifying the interface to better control the mixing of nanospray ions with the afterglow and by enhancing ion delivery to the MS.

To estimate the extent of Ba¹⁸OH⁺ interference in ICP-nanospray-MS, we monitored m/z 151 corresponding to ¹³⁴BaOH⁺ which is free form BaF⁺ contributions. Infusion of pure solvent led to baseline intensities of 1.2 x 10⁵ cps at m/z 151 and 4 x 10⁴ cps at m/z 157. Considering abundances of 3.37% for ¹³⁴Ba and 0.2% for ¹⁸O, we estimate that only 18% of the intensity at m/z 157 is contributed by Ba¹⁸OH⁺. We attribute the remaining fraction to BaF⁺ background. The low extent of BaOH⁺ interference in post-plasma chemical ionization reduces the need for MS/MS and gas dilution, in turn allowing facile detection of BaF⁺ with unit resolution single quadrupole instruments at increased sensitivities.

Table 3 also shows a better LOD using ICP-nanospray-MS compared to other ICP-MS methods. However, the extent of improvement in LOD does not scale with the enhancement of sensitivity using ICP-nanospray-MS. This is because LOD is largely determined by a relatively high background equivalent concentration (BEC). As noted above, only a small portion of the background is attributed to Ba¹⁸OH⁺. BEC contributions from F contamination may originate from a wide range of sources, including gases and gas handling equipment, solvents and liquid path materials, as well as the nanospray electrolyte. Nevertheless, the low contribution of BaOH⁺ to the intensity at the analytical ion m/z signifies a major enhancement relative to other ICP-MS methods and indicates the potential of the ICP-nanospray-MS for enhanced LOD upon reducing F contamination.

While most methods in recent years have focused on polyatomic positive ion detection for F analysis using ICP, it is noteworthy to also consider the studies devoted to negative ion detection given the high electron affinity of F. In particular, negative mode ICP-MS where F⁻ is generated via electron capture by F atoms in the supersonic expansion of plasma into the vacuum of the MS has shown a promising sensitivity of 60 cps/ppb.³⁸ However, ¹⁸OH⁻ ion creates a major isobaric interference for this approach, resulting in significantly higher LOD of 110 ng/mL compared to those in Table 3. Inspired by the potential for high sensitivity, we have also investigated F⁻ detection in the atmospheric pressure afterglow of ICP.³⁹ However, these efforts did not yield any detectable ions in samples containing up to 9500 ng/mL F, suggesting rapid ion-neutral reactions of plasma-produced F⁻, leading to its neutralization at atmospheric pressure. We note that this neutralization mechanism could be a contributor to the formation of HF detected in the current report. Overall, the positive mode chemical ionization reported above using nanospray-generated reagent ions shows an advantage over other methodologies for improving on-line mass spectrometric F detection of LC eluates.

Matrix effects in ionization. To evaluate the robustness of the chemical ionization for elemental analysis of F, we selected a number of interfering elements that may be encountered in environmental and biological applications. In particular, we explored the effects of carbon loading from matrix, as well as effects of analytes that contain S, P, and Cl. The latter elements were selected because of potential to form acidic plasma products which may compete with HF for reactions with the reagent ions. The results in Figure 9 show minimal effects from C, S, and P in the examined concentration range. Chlorine concentrations up to at 145 μM (5075 ng/mL) are well tolerated by the ionization method, however, 32% and 42% ion suppressions are observed at 246 and 480 μM (8610 and 16800 ng/mL) Cl concentrations, respectively. These findings suggest that large extent of HCl formed via plasma reactions of chlorinated compounds interferes with the chemical ionization of HF to BaF⁺. Co-elution with organochlorines can be minimized by separations prior to the ICP. Notably, high tolerance to matrix composed of organic compounds with CHNO elements suggests that low concentrations of fluorinated compounds could be quantitatively

detected using ICP-nanospray-MS via sample pre-concentration and LC separations where co-elution with major organic components of the sample may occur.

Conclusions

Formation of polyatomic ions by nanospray-induced chemical ionization in the ICP afterglow offers a substantial improvement in sensitivity for F elemental analysis compared to ion formation inside the plasma implemented in conventional ICP-MS methods. We have demonstrated that close to two orders of magnitude sensitivity improvement is readily achieved relative to ICP-MS/MS techniques. Notably, this improvement was observed using a dated mass spectrometer with a 0.25 mm ion sampling orifice. Recent advances in atmospheric ion sampling via larger orifice sizes and high efficiency ion guides have drastically improved performance of mass spectrometers. Thus, additional major improvements in sensitivity are expected upon use of advanced mass spectrometers. Relatedly, low-temperature post-plasma chemical ionization facilitates use of various molecular mass spectrometers (designed for molecular ion sources such as electrospray ionization) for elemental analyses.

Fundamentally, the post-plasma chemical ionization offers a tunable ionization chemistry where a range of reagent ions are supplied by nanospray. Our studies in this report show one example of versatility of this approach to improve analytical performance where barium-based reagent ions produced an order of magnitude enhancement in sensitivity compared to sodium-based ions because of reduced clustering. The results also indicated that the most abundant ions (BaCH₃CO₂⁺ and BaHCO₂⁺) observed in the spectrum are poor reagent ions for BaF⁺ production. Therefore, further enhancement in sensitivity is expected upon selecting electrolytes that largely create efficient reagent ions in the electrospray process. Similarly, the approach opens avenues to develop ion-neutral reactions that increase ionization robustness to matrix effects. We also note that the chemical ionization can substantially reduce isobaric interferences. Our investigations suggest that BaOH⁺ is a minor isobaric interference in the chemical ionization approach while it presents a major hurdle in other ICP-MS techniques.

Author Contributions

The studies were conceptualized and designed by SW, KZ, JEL, and KJ. All authors contributed to data collection and data analysis. SW and KJ wrote the original draft. All authors contributed to editing and review of the final draft.

Conflicts of Interest

SW, KZ, JEL, and KJ are co-inventors on a pending patent application based on the technique presented in this report. KJ is a co-inventor on a granted US Patent and a pending European patent application related to the technique presented in this report. JT declares no conflicts of interest.

Acknowledgements

This material is based upon work supported by National Science Foundation (NSF) under Grant CHE-1904835. We thank Perkin Elmer Inc. for the loan of the ICP generator used in these studies. We are particularly grateful to Dr. Hamid Badiei and Dr. Dickson Cheung of PerkinElmer for technical support of the plasma generator. We thank Meinhard Inc. for providing the sample introduction components used in this study. We are thankful to Dr. Frenio Redeker of Georgetown University for suggestions in computational investigations.

References

- 1 P. Richardson, Expert Opin. Drug Discov., 2021, 16, 1261–1286.
- 2 M. Inoue, Y. Sumii and N. Shibata, ACS Omega, 2020, 5, 10633–10640.
- 3 S. P. Gupta, Lett. Drug Des. Discov., 2019, 16, 1089–1109.
- 4 A. Banerjee and Y. Liu, *Langmuir*, 2021, **37**, 8937–8944.
- 5 N. Xu, J. Shi, G. Liu, X. Yang, J. Zheng, Z. Zhang and Y. Yang, J. Power Sources Adv., 2021, 7, 100043.
- 6 O. S. Arvaniti and A. S. Stasinakis, Sci. Total Environ., 2015, **524–525**, 81–92.
- 7 Z. Wang, J. C. DeWitt, C. P. Higgins and I. T. Cousins, *Env. Sci Technol*, 2017, **51**, 2508–2518.
- 8 Y. Gong, J. Chen, Y. Shi, H.-K. Lim, N. Weng and R. Salter, Anal. Chem., 2017, 89, 8399-8404.
- 9 R. K. Singh, S. Fernando, S. F. Baygi, N. Multari, S. M. Thagard and T. M. Holsen, *Environ. Sci. Technol.*, 2019, **53**, 2731–2738.
- 10 R. Gonzalez de Vega, A. Cameron, D. Clases, T. M. Dodgen, P. A. Doble and D. P. Bishop, J. Chromatogr. A, 2021, 1653, 462423.
- 11 B. González-Gaya, N. Lopez-Herguedas, D. Bilbao, L. Mijangos, A. M. Iker, N. Etxebarria, M. Irazola, A. Prieto, M. Olivares and O. Zuloaga, *Anal. Methods*, 2021, **13**, 1876–1904.
- 12 J. Liigand, T. Wang, J. Kellogg, J. Smedsgaard, N. Cech and A. Kruve, Sci. Rep., 2020, 10, 5808.
- 13 J. R. Enders, G. M. O'Neill, J. L. Whitten and D. C. Muddiman, *Anal. Bioanal. Chem.*, 2022, **414**, 1227–1234.
- 14 B. Klencsár, S. Li, L. Balcaen and F. Vanhaecke, TrAC Trends Anal. Chem., 2018, 104, 118–134.
- 15 L. Cid-Barrio, F. Calderón-Celis, P. Abásolo-Linares, M. L. Fernández-Sánchez, J. M. Costa-Fernández,
- J. R. Encinar and A. Sanz-Medel, TrAC Trends Anal. Chem., 2018, 104, 148–159.
- 16 R. C. Fry, S. J. Northway, R. M. Brown and S. K. Hughes, *Anal. Chem.*, 1980, **52**, 1716–1722.
- 17 P. Maung and D. Beauchemin, J. Anal. At. Spectrom., 2020, 35, 1097–1102.
- 18 P. Maung and D. Beauchemin, J. Anal. At. Spectrom., 2021, 36, 1104–1111.
- 19 Z. Qin, D. McNee, H. Gleisner, A. Raab, K. Kyeremeh, M. Jaspars, E. Krupp, H. Deng and J. Feldmann, *Anal. Chem.*, 2012, **84**, 6213–6219.

- 20 M. Metzger, P. Ley, M. Sturm and B. Meermann, Anal. Bioanal. Chem., 2019, 411, 4647–4660.
- 21 A. Akhdhar, M. Schneider, A. Orme, L. Schultes, A. Raab, E. M. Krupp, J. P. Benskin, B. Welz and J. Feldmann, *Talanta*, 2020, **209**, 120466.
- 22 A. Akhdhar, M. Schneider, S. Hellmann, A. Orme, E. Carasek, E. M. Krupp and J. Feldmann, *Talanta*, 2021, **227**, 122190.
- 23 H. Niu and R. S. Houk, Spectrochim. Acta B, 1996, 51, 779–815.
- 24 X. Bu, T. Wang and G. Hall, J. Anal. At. Spectrom., 2003, 18, 1443–1451.
- 25 W. Guo, L. Jin, S. Hu and Q. Guo, J. Agric. Food Chem., 2017, 65, 3406–3412.
- 26 Y. Zhu, K. Nakano and Y. Shikamori, Anal. Sci., 2017, 33, 1279–1284.
- 27 N. L. A. Jamari, J. F. Dohmann, A. Raab, E. M. Krupp and J. Feldmann, J. Anal. At. Spectrom., 2017, 32, 942–950.
- 28 N. L. A. Jamari, A. Behrens, A. Raab, E. M. Krupp and J. Feldmann, *J. Anal. At. Spectrom.*, 2018, **33**, 1304–1309.
- 29 J. E. Lesniewski, K. Zheng, P. Lecchi, D. Dain and K. Jorabchi, *Anal. Chem.*, 2019, **91**, 3773–3777.
- 30 K. Zheng, J. E. Lesniewski, M. J. Dolan, W. Li, T. T. Metallo and K. Jorabchi, *Anal. Chem.*, 2020, **92**, 10129–10137.
- 31 M. J. Frisch, G. W. Trucks, H. B. Schlegel, G. E. Scuseria, M. A. Robb, J. R. Cheeseman, G. Scalmani, V. Barone, G. A. Petersson, H. Nakatsuji, X. Li, M. Caricato, A. V. Marenich, J. Bloino, B. G. Janesko, R.
- Gomperts, B. Mennucci, H. P. Hratchian, J. V. Ortiz, A. F. Izmaylov, J. L. Sonnenberg, Williams, F. Ding,
- F. Lipparini, F. Egidi, J. Goings, B. Peng, A. Petrone, T. Henderson, D. Ranasinghe, V. G. Zakrzewski, J.
- Gao, N. Rega, G. Zheng, W. Liang, M. Hada, M. Ehara, K. Toyota, R. Fukuda, J. Hasegawa, M. Ishida, T.
- Nakajima, Y. Honda, O. Kitao, H. Nakai, T. Vreven, K. Throssell, J. A. Montgomery Jr., J. E. Peralta, F.
- Ogliaro, M. J. Bearpark, J. J. Heyd, E. N. Brothers, K. N. Kudin, V. N. Staroverov, T. A. Keith, R.
- Kobayashi, J. Normand, K. Raghavachari, A. P. Rendell, J. C. Burant, S. S. Iyengar, J. Tomasi, M. Cossi,
- J. M. Millam, M. Klene, C. Adamo, R. Cammi, J. W. Ochterski, R. L. Martin, K. Morokuma, O. Farkas, J.
- B. Foresman and D. J. Fox, Gaussian 16 Rev. C.01, Wallingford, CT, 2016.

- 32 W. Guo, X. Lin, L. Jin and S. Hu, J. Food Compos. Anal., 2020, 86, 103378.
- 33 N. L. A. Jamari, J. F. Dohmann, A. Raab, E. M. Krupp and J. Feldmann, *Anal. Chim. Acta*, 2019, **1053**, 22–31.
- 34 J. Sunner, M. G. Ikonomou and P. Kebarle, Anal. Chem., 1988, 60, 1308–1313.
- 35 S. G. Lias, J. E. Bartmess, J. F. Liebman, J. L. Holmes, R. D. Levin and W. G. Mallard, *J. Phys. Chem. Ref. Data*, 1988, **17**, Supplement 1.
- 36 R. R. Squires, Int. J. Mass Spectrom. Ion Process., 1992, 117, 565-600.
- 37 O. W. Wheeler, D. R. Carl, T. E. Hofstetter and P. B. Armentrout, *J. Phys. Chem. A*, 2015, **119**, 3800–3815.
- 38 J. E. Fulford and E. S. K. Quan, Appl. Spectrosc., 1988, 42, 425–428.
- 39 J. E. Lesniewski, W. P. McMahon and K. Jorabchi, *J Anal. At. Spectrom.*, 2018, **33**, 1981–1992.
- 40 N. Yamada, Agilent 8800 ICP-QQQ Application Handbook, Agilent Technologies, 2013, 33-34.

Table 1. Reaction energies for gaseous $BaF^{\scriptscriptstyle +}$ formation calculated at $\omega B97xD/aug\text{-}cc\text{-}pVTZ$ level of theory

Reaction	ΔH _{0 K} (kJ/mol)	ΔH _{298 K} (kJ/mol)	ΔG _{298 K} (kJ/mol)
$HF + BaHCO_2^+ \rightarrow BaF^+ + HCO_2H$	26.8	24.1	19.9
$HF + BaCH_3CO_2^+ \rightarrow BaF^+ + CH_3CO_2H$	41.1	37.4	36.6
$HF + BaNO_2^+ \rightarrow BaF^+ + HNO_2$	-19.0	-22.2	-24.1
$HF + BaNO_3^+ \rightarrow BaF^+ + HNO_3$	21.8	18.7	14.0
$HF + BaHCO_3^+ \rightarrow BaF^+ + H_2CO_3$	42.9	39.6	38.4
$H_2CO_3 \rightarrow H_2O + CO_2$	-24.3	-17.1	-58.7
$HF + BaHCO_3^+ \rightarrow BaF^+ + H_2O + CO_2$	18.6	22.5	-20.3
$HF + BaOH^+ \rightarrow BaF^+ + H_2O$	-42.3	-43.1	-44.3
$HF + Ba(H_2O)_3^{2+} \rightarrow BaF(H_2O)_2^{+} + H_3O^{+}$	-109.8	-115.7	-95.2

 $\Delta H_{0\,K}$ reflects zero-point corrected electronic energies

Table 2. Uniformity of fluorine response factors among fluorinated compounds

		Normalized			Normalized
Compound	F (μΜ)	Response Factor*	Compound	F (μΜ)	Response Factor*
CI NO NO PER	46.6	0.96 ± 0.04	Flecainide	74.9	0.97 ± 0.04
Fluconazole	71.0	0.99 ± 0.06	Paroxetine	32.6	1.06 ± 0.07
HO N N F N N S N S S S F F N S S F S F N S S S S	59.2	0.99 ± 0.05	CI OH	31.5	1.02 ± 0.07
Fluoxetine	64.9	1.05 ± 0.07	Haloperidol CI N N N N Midazolam	43.7	0.95 ± 0.03
N N N N N N N N N N N N N N N N N N N	60.0	0.96 ± 0.05	F F F Fluvoxamine	75.6	1.00 ± 0.05

^{*}F response factors are normalized to the average value among all compounds. Standard deviations of the normalized response are calculated based on triplicate flow injections. A sampling orifice size of 3 mm and N_2 gas flow rate of 2.6 L/min in the venturi tee were used for these experiments.

Table 3. Comparison of the analytical performances for F detection using BaF⁺ as analytical ion

Instrument	Sensitivity (cps/ppb)	BEC (ng/mL F)	LOD (ng/mL F)	Contribution of counting statistics to net signal reproducibility for a 100 ng/mL F solution (%RSD) ^a
ICP-MS/MS ²⁷	3.2	607^{b}	43	28.7 %
ICP-MS/MS ²⁵	1.6	21	22	13.3 %
ICP-MS/MS ²⁶	2	400	60	30.0 %
$ICP-MS^{32}$	0.4	30	32	28.3 %
ICP-MS/MS ⁴⁰	4.1	230	27	16.6 %
ICP-nanospray-MS	281	191	11	1.9 %

^a the values are calculated using $\frac{100 \times \sqrt{I_s + I_b}}{I_s - I_b}$ where I_s and I_b are the average number of ions detected in 500 ms for 100 ng/mL F solution and blank, respectively. The average ion counts are calculated based on BEC and sensitivity values.

^b calculated from the data in the reference

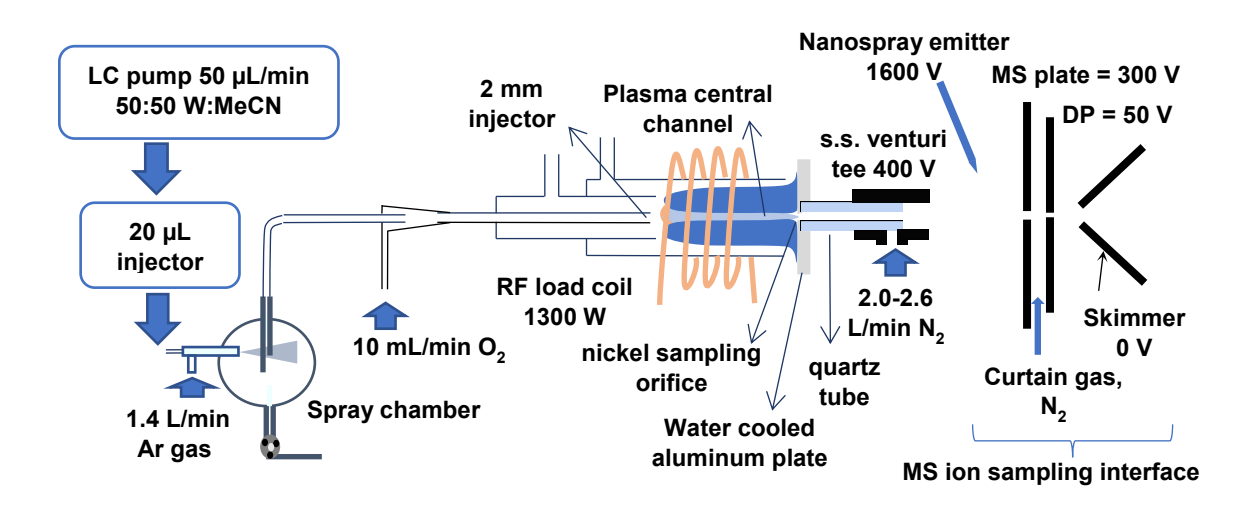


Figure 1. Schematic of experimental setup and the main operating parameters for nanospray-induced chemical ionization in afterglow of an ICP. Diagram is not to scale.

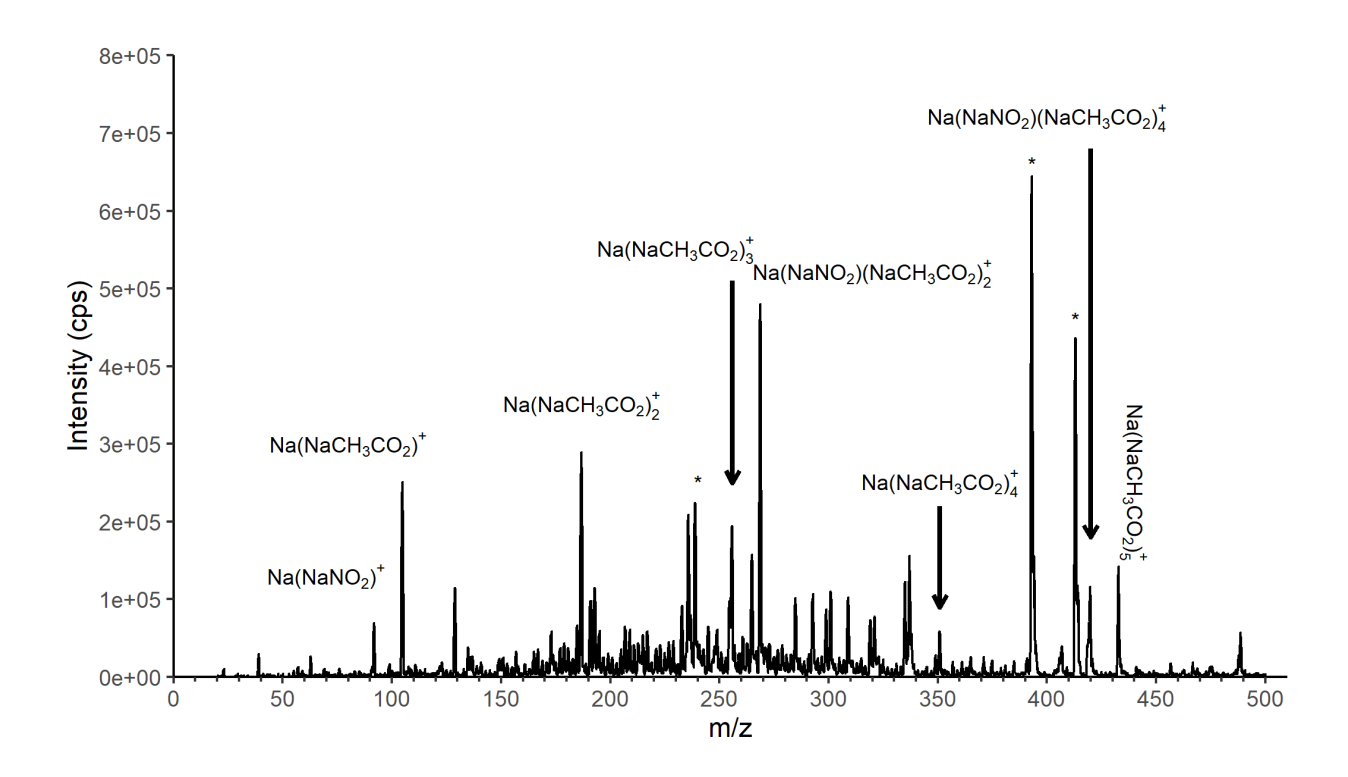


Figure 2. Major ions detected from interaction of 1 mM sodium acetate nanospray with post-plasma flow emerging from the venturi tee. Na(NaCH₃CO₂)_n⁺ ions originate from the nanospray. Reactions of these ions with plasma-produced HNO₂ leads to clusters where acetate is replaced with nitrite. The asterisks (*) are attributed to commonly observed species with electrospray ionization at m/z 236 ([M+Na]⁺, n-butyl benzenesulfunamide, 393 ([M+Na]⁺, dioctyl adipate, and 413 ([M+Na]⁺, diisooctyl phthalate). A sampling orifice size of 4 mm and N₂ gas flow rate of 2.1 L/min introduced into the venturi tee were utilized in these experiments.

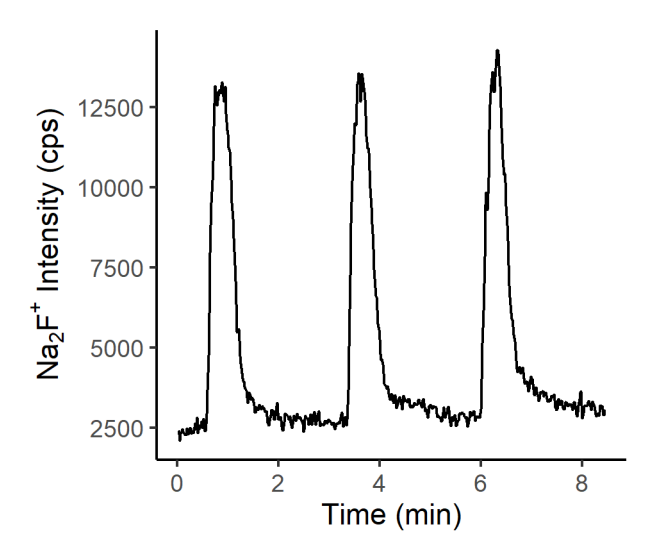


Figure 3. Detection of Na_2F^+ at m/z 65 using 1 mM sodium acetate nanospray electrolyte for afterglow ionization and triplicate flow injections of 20 μ M F using fluconazole as analyte. A sampling orifice size of 4 mm and N_2 gas flow rate of 2.1 L/min introduced into the venturi tee were utilized in these experiments.

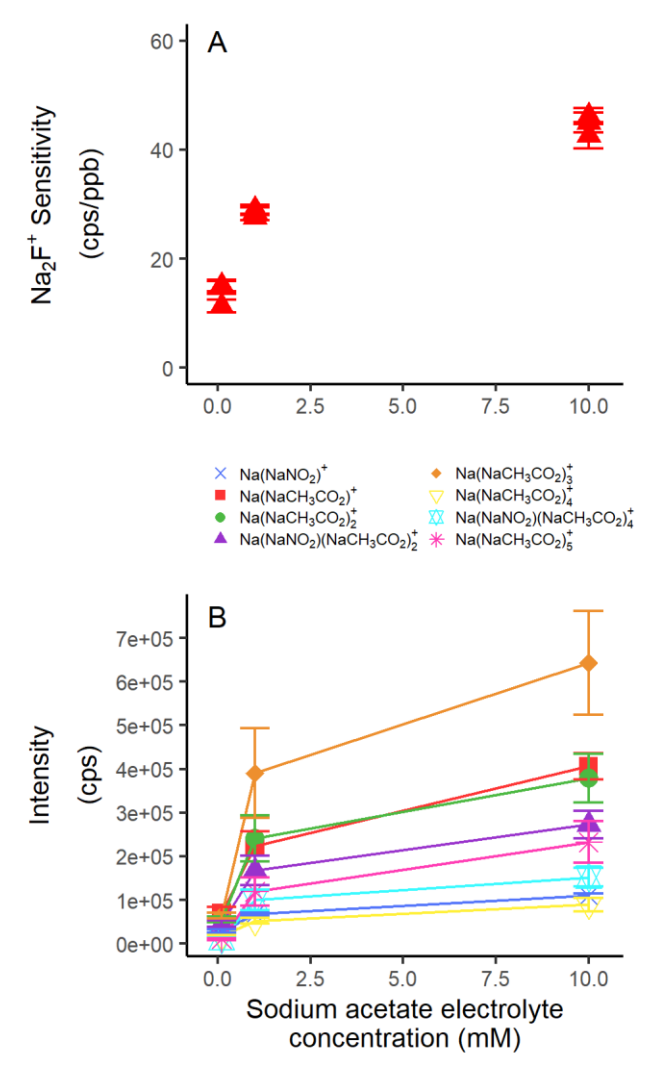


Figure 4. A) Effect of sodium acetate nanospray electrolyte concentration (100 μm-10 mM) on F detection sensitivity in ICP-nanospray-MS using Na₂F⁺ as analytical ion. Flow injections of 20 μM F in the form of fluconazole were utilized for sensitivity measurements. Each triangle represents a new nanospray emitter to capture effect of emitter size and positioning reproducibility. Error bars represent standard deviations of sensitivity measurements based on triplicate flow injections using the same emitter. **B)** Effect of sodium acetate nanospray electrolyte concentration on background ion intensities in ICP-nanospray-MS. Error bars denote standard deviations of ion intensities using three different nanospray emitters. A sampling orifice size of 4 mm and a N₂ gas flow rate of 2.1 L/min introduced into the venturi tee were utilized in these experiments.

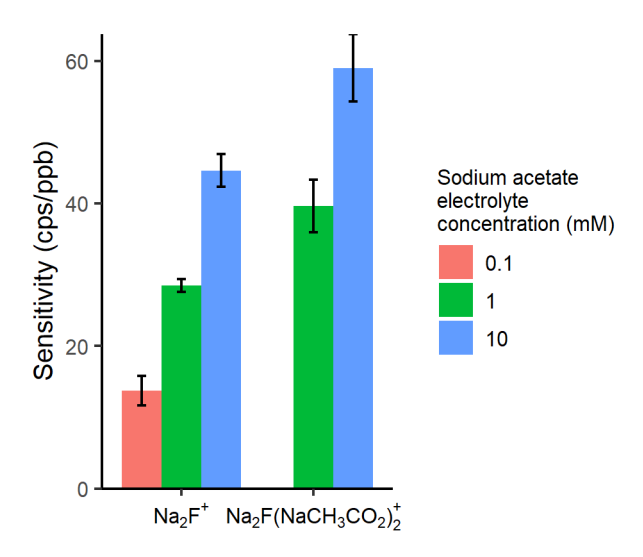


Figure 5: Detection sensitivities for Na_2F^+ and $Na_2F(CH_3CO_2)_2^+$ determined from peak heights in flow injections of 20 μ M F as fluconazole. Error bars denote standard deviation of measurements using three different emitters and triplicate flow injections per emitter (n=9). A sampling orifice size of 4 mm and a N_2 gas flow rate of 2.1 L/min introduced into the venturi tee were utilized in these experiments.

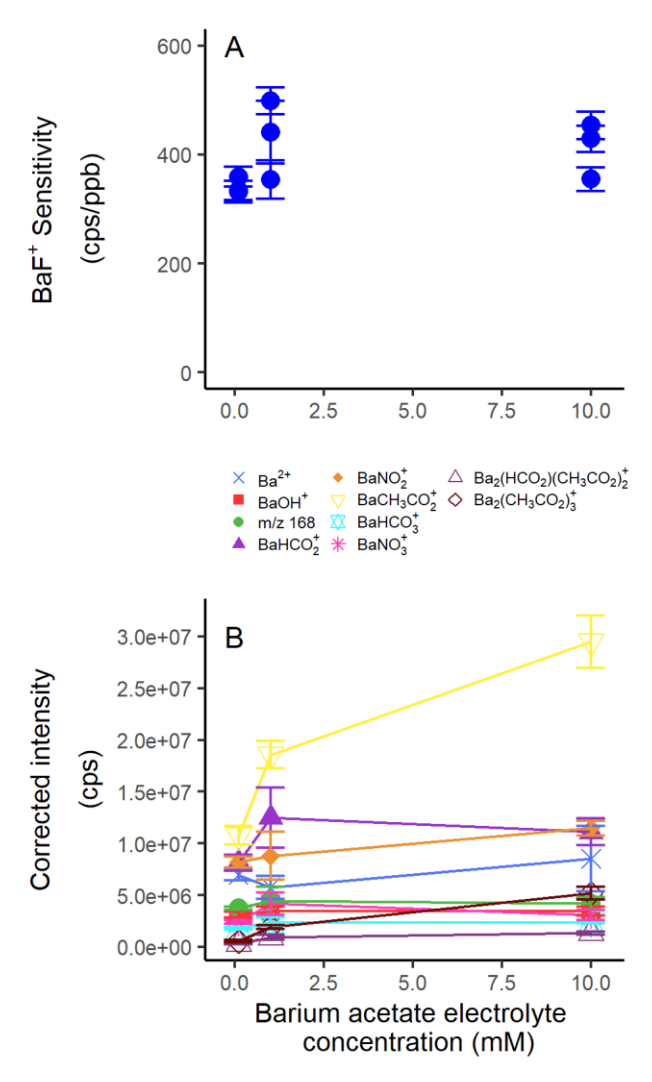


Figure 6. A) Effect of barium acetate concentration (0.1 mM-10 mM) in nanospray on F detection sensitivity in ICP-nanospray-MS using BaF⁺ as analytical ion. Flow injections of 20 μM F in the form of fluconazole were utilized for sensitivity measurements. Each dot represents a new nanospray emitter. Error bars represent standard deviations of sensitivity measurements based on triplicate flow injections using the same emitter. **B)** Effect of barium acetate concentration in nanospray on background ion intensities in ICP-nanospray-MS. Error bars are standard deviations of intensities from three measurements each using a different nanospray emitter. Ion intestines were measured by detuning the lens between the second and third quadrupoles of the instrument to avoid detector saturation. The measured intensities were then corrected after data acquisition. A sampling orifice size of 4 mm and a N₂ gas flow rate of 2.1 L/min introduced into the venturi tee were utilized in these experiments.

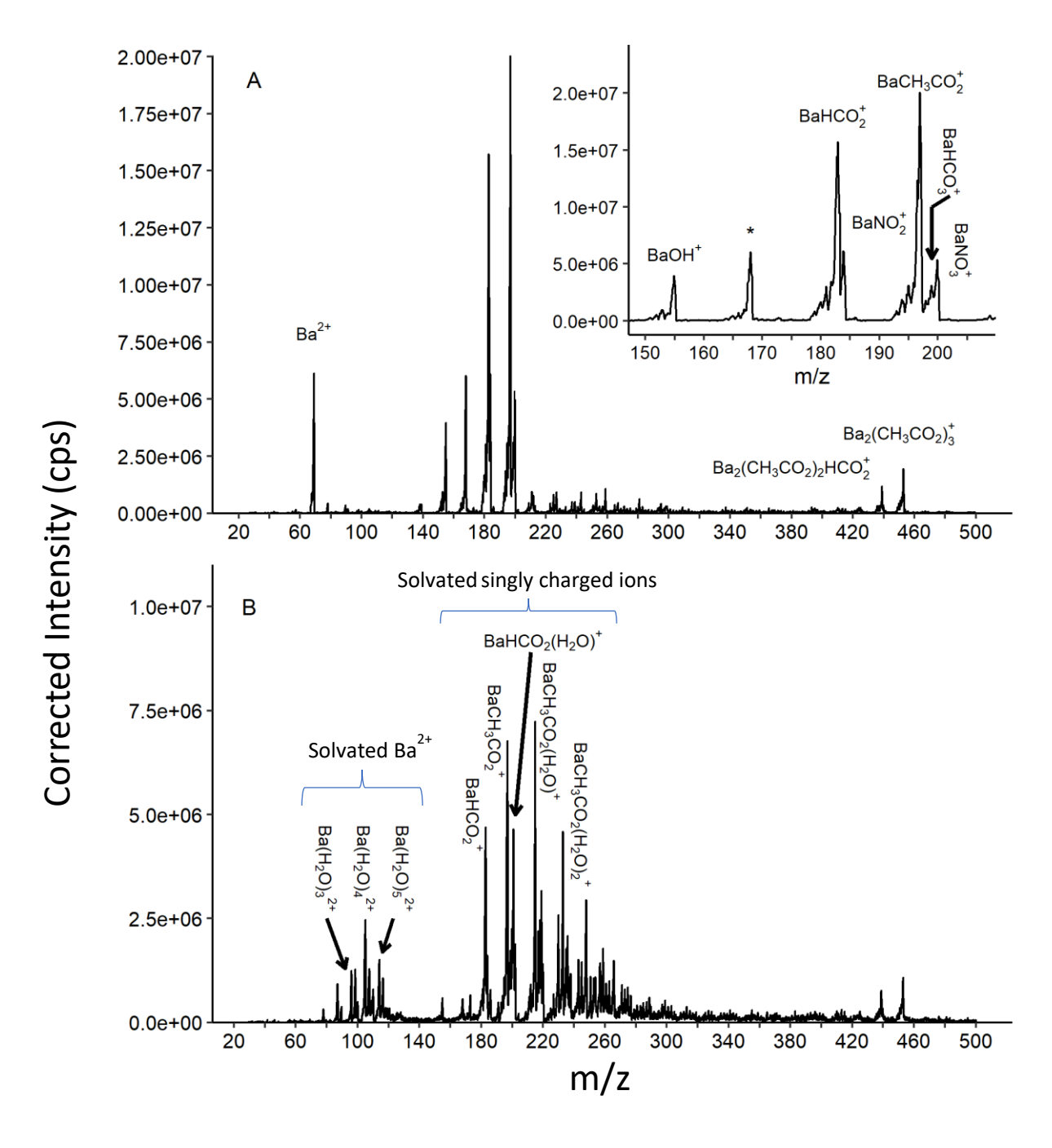


Figure 7. Background ion spectra from interaction of 1 mM barium acetate nanospray ions with post-plasma flow using A) declustering potential of 50 V, and B) declustering potential of 10 V (soft ion sampling). Ion intestines were measured by detuning the lens between the second and third quadrupoles of the instrument to avoid detector saturation. The measured intensities were then corrected after data acquisition. The correction factor was determined using intensities for m/z 157 with both normal and

detuned settings. Asterisk (*) in panel A denotes an unidentified ion at m/z 168. A sampling orifice size of 4 mm and a N_2 gas flow rate of 2.1 L/min introduced into the venturi tee were utilized in these experiments.

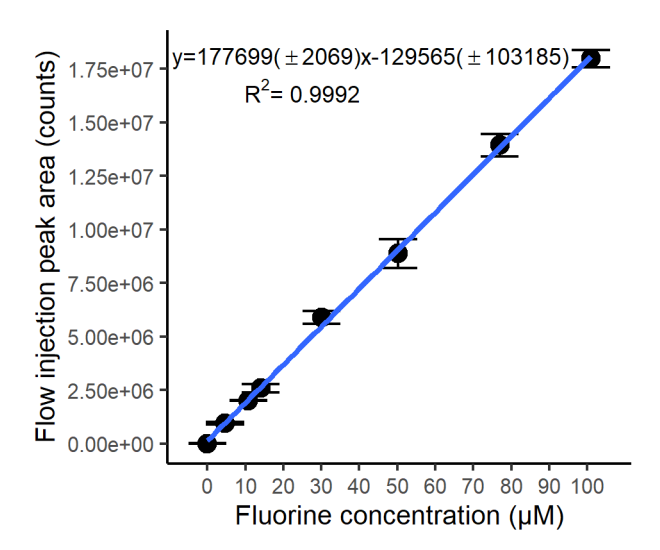


Figure 8. Calibration curve via flow injections of fluconazole using BaF⁺ as analytical ion measured at m/z 157. Error bars represent standard deviations of peak areas based on triplicate injections of standards and 6 injections of blank. Standard errors for slope and intercept are shown in parentheses. A sampling orifice size of 3 mm and a N₂ gas flow rate of 2.6 L/min introduced into the venturi tee were utilized in these experiments.

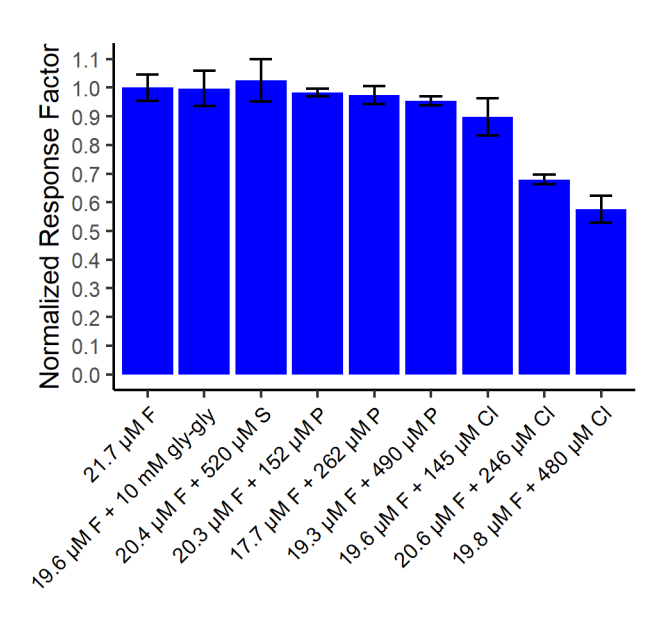


Figure 9. Effect of concomitant elements on BaF⁺ response factor. Response factors (peak area per mol of F) are normalized to that of the sample with only F as fluconazole. P, S, and Cl are introduced in the forms of glyphosate, thiourea, and sucralose, respectively. Error bars represent standard deviations of normalized response factors based on triplicate flow injections. A sampling orifice size of 3 mm and a N₂ gas flow rate of 2.6 L/min introduced into the venturi tee were utilized in these experiments.

Electronic Supplementary Information

Elemental Detection of Fluorochemicals by Nanospray-Induced Chemical Ionization in Afterglow of an Inductively Coupled Plasma

Samuel White, Kunyu Zheng, a Jordan Tanen, Joseph E. Lesniewski, and Kaveh Jorabchi

Department of Chemistry, Georgetown University, Washington, D.C. 20057, United States

β Currently at Wilson Sonsini Goodrich & Rosati, Washington, D.C. 20006, United States



Figure S1. Ionization area of the ICP-nanospray-MS setup, showing the cooled aluminum plate of the ICP interface coupled to a quartz plasma sampling tube, a venturi tee, and a nanospray emitter.

^{*} Corresponding author, kj256@georgetown.edu

^α Currently at AbbVie Inc., North Chicago, IL, 60064, United States

Examination of soft ion sampling spectrum. To investigate the effect of fragmentation during ion sampling on appearance of BaOH⁺ and m/z 168, we collected a background spectrum with softer sampling by lowering declustering potential (DP) from 50 V to 10 V. Figure S2 provides annotation of ions with intensities ≥ 320000 cps. This intensity threshold was established based on the lowest intensity hydrated barium species detected in the spectra, namely BaOH(H₂O)⁺, and corresponds to 4.4% of that of the most intense ion in the spectrum, providing a reasonable cut off threshold for identification of potential reagent ions. A list of ions and their intensities is tabulated in Table S1.

As noted in Figure S2 and Table S1, several solvated species of each core ion are detected. The solvation is dramatically reduced via ion activation at declustering potential of 50 V (see Figure 7A in the article). Therefore, to compare the prevalence of core ions between declustering potentials of 50 and 10 V, we utilized an aggerate intensity equal to the sum of intensities of each core ion and its solvated species. For example, for the core ion BaOH⁺ three solvated ions have been detected in soft sampling conditions, BaOH⁺, BaOH(H₂O)⁺, and BaOH(H₂O)₂⁺, with intensities of 596124, 664138, and 492102 cps, respectively, resulting in total prevalence of 1752364 for this core ion.

Table S2 summarizes such aggregate intensities for each core ion at both soft (10 V DP) and harsh (50 V DP) ion sampling conditions. The ratio of the intensities between the two sampling conditions provides a metric for the effect of ion sampling on prevalence of each core ion. Notably, only BaOH⁺ and m/z 168 show a significant improvement in prevalence when harsh ion sampling is utilized, supporting the hypothesis that these species are mainly products of fragmentation in ion sampling.

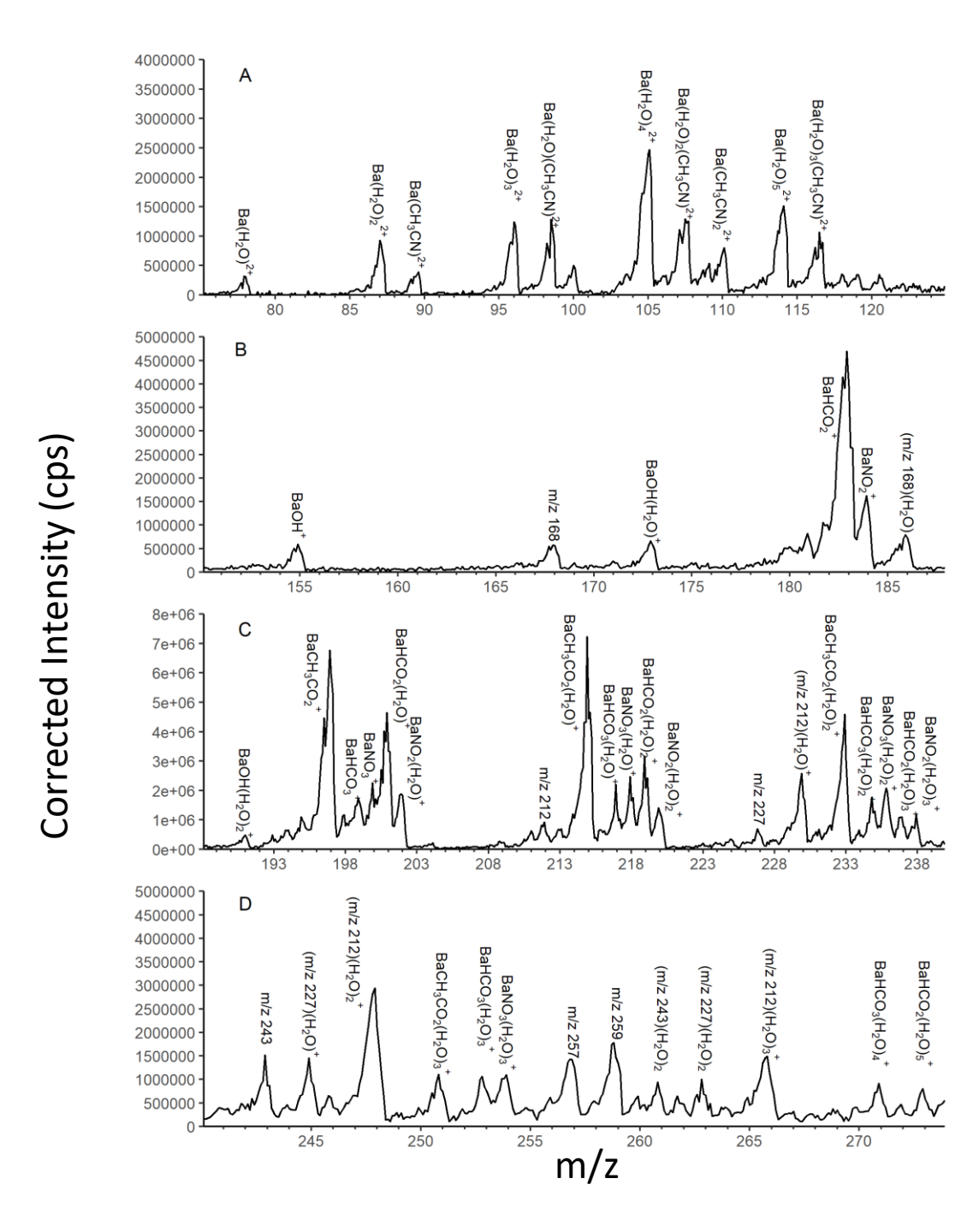


Figure S2. Proposed ion formulas in background spectrum of ICP-nanospray-MS using soft ion sampling conditions (declustering potential of 10 V) and 1 mM barium acetate as the nanospray electrolyte. Note that the total spectrum is split to four m/z ranges via panels A to D for ease of presentation. A sampling orifice size of 4 mm and a N_2 gas flow rate of 2.1 L/min introduced into the venturi tee were utilized in these experiments.

Table S1. Ion intensities using soft ion sampling conditions

m/z	Ion	Intensity (cps)	m/z	Ion	Intensity (cps)
78	$\overline{\mathrm{Ba}(\mathrm{H_2O})^{+2}}$	320067	217	BaHCO ₃ (H ₂ O) ⁺	2208460
87	$Ba(H_2O)_2^{+2}$	928193	218	$BaNO_3(H_2O)^+$	2472515
89.5	$Ba(CH_3CN)^{2+}$	388081	219	$BaHCO_2(H_2O)_2^+$	3164659
96	$Ba(H_2O)_3^{2+}$	1244259	220	$BaNO_2(H_2O)_2^+$	1408293
98.5	$Ba(H2O)(CH3CN)^{2+}$	1284267	227	Unknown	692144
105	$Ba(H_2O)_4^{2+}$	2472515	230	$(m/z 212)(H_2O)$	2584538
107.5	$Ba(H_2O)_2(CH_3CN)^{2+}$	1288268	233	$BaCH_3CO_2(H_2O)_2^+$	4592956
110	$Ba(CH_3CN)_2^{2+}$	804167	235	$BaHCO_3(H_2O)_2^+$	1768368
114	$Ba(H_2O)_5^{2+}$	1516316	236	$BaNO_3(H_2O)_2^+$	2080433
116.5	$Ba(H_2O)_3(CH_3CN)^{2+}$	1068222	237	$BaHCO_2(H_2O)_3^+$	1096228
155	$BaOH^+$	596124	238	$BaNO_2(H_2O)_3^+$	1172244
168	Unknown	564117	243	Unknown	1516315
173	$BaOH(H_2O)^+$	664138	245	$(m/z 245)(H_2O)$	1456303
183	$\mathrm{BaHCO_2}^+$	4700979	248	$(m/z 212)(H_2O)_2$	2944613
184	$\mathrm{BaNO_2}^+$	1624338	251	$BaCH_3CO_2(H_2O)_3^+$	1104230
186	$(m/z 168)(H_2O)$	796166	253	$BaHCO_3(H_2O)_3^+$	1068222
191	$BaOH(H_2O)_2^+$	492102	254	$BaNO_3(H_2O)_3^+$	1100229
197	$BaCH_3CO_2^+$	6773410	257	Unknown	1432298
199	$\mathrm{BaHCO_3}^+$	1736362	259	Unknown	1784372
200	$\mathrm{BaNO_3}^+$	2260471	261	$(m/z 243)(H_2O)$	944190
201	$BaHCO_2(H_2O)^+$	4648968	263	$(m/z 227)(H_2O)_2$	1004205
202	$BaNO_2(H_2O)^+$	1888393	266	$(m/z 212)(H_2O)_3$	1492311
212	Unknown	924192	271	$BaCH_3CO_2(H_2O)_4^+$	912190
215	$BaCH_3CO_2(H_2O)^+$	7233506			

Table S2. Core ion aggregate intensities

Core Ion	Aggregate Intensity in Soft Sampling (cps)	Aggregate Intensity in Harsh Sampling (cps)	Ratio of Harsh to Soft Sampling Intensities
Ba^{2+}	11314355	6141850	0.5
$BaOH^+$	1752364	3965969	2.3
m/z 168	1360283	6033828	4.4
BaHCO ₂ ⁺	13610834	15730133	1.2
$\mathrm{BaNO_2}^+$	6093268	6116130	1.0
BaCH ₃ CO ₂ ⁺	19704102	20035601	1.0
BaHCO ₃ ⁺	7693602	3112077	0.4
$\mathrm{BaNO_3}^+$	7913648	5352257	0.7
m/z 212	7945654	779305	0.1
m/z 227	3152652	936194	0.3
m/z 243	2460505	938767	0.4
m/z 257	1432298	Not Detected	N/A
m/z 259	1784372	1085369	0.6

The ions with assigned formulas account for 79% and 86% of the total major ion intensities in soft and harsh ion sampling conditions, respectively.

Optimized geometries and energies (Hartree/particle) at $\omega B97xD/aug\text{-cc-pVTZ}$ level of theory:

BaCH₃CO₂⁺

Eleme	ent Coordinates (Angstroms)					
X	Y Z					
Ba	-1.054308 -0.000016 0.001278					
O	1.126496 1.100688 -0.006516					
O	1.126475 -1.100497 -0.006600					
C	1.766922 0.000106 -0.012420					
C	3.257698 -0.000044 0.001390					
Н	3.643663 0.899460 -0.469062					
Н	3.643281 -0.896650 -0.474952					
Н	3.582826 -0.003820 1.043543					
Rotatio	onal symmetry number =	1				
Zero-p	oint correction=	0.050552				
Sum o	Sum of electronic and zero-point Energies= -253.834193					
Sum o	Sum of electronic and thermal Energies= -253.828013					
Sum o	Sum of electronic and thermal Enthalpies= -253.827069					
Sum o	f electronic and thermal Free Energies=	-253.867057				

BaF ⁺				
Element Coordinates (Angstroms)				
X Y Z				
F 0.000000 0.000000 -1.824729				
Ba 0.000000 0.000000 0.293260				
Rotational symmetry=	1			
Zero-point correction=	0.001198			
Sum of electronic and zero-point Energies=	-125.224971			
Sum of electronic and thermal Energies= -125.22240				
Sum of electronic and thermal Enthalpies=	-125.221460			

Sum of electronic and thermal Free Energies=

-125.248642

BaF(H₂O)₂⁺

Element Coordinates (Angstroms)					
X	Y	Z			
Ba		-0.000000	-0.564054	0.065697	
O		-2.200676	0.797206	-0.563469	
Н		-1.945093	1.620238	-0.125336	
Н		-3.062469	0.930024	-0.960414	
O		2.200676	0.797204	-0.563470	
Н		1.945094	1.620236	-0.125335	
Н		3.062470	0.930022	-0.960417	
F		0.000002	1.525694	0.834223	
Rotatio	nal	symmetry=			1
Zero-point correction=					0.051000
Sum of electronic and zero-point Energies=					-278.132649
Sum of electronic and thermal Energies=				-278.124440	
Sum of electronic and thermal Enthalpies=				-278.123496	
Sum of electronic and thermal Free Energies=				-278.166896	

$Ba(H_20)_3^{+2}$

Element Coordinates (Angstroms)					
X	Y	Z			
Ba		0.000245	-0.000525	-0.279599	
O		-2.313402	-1.090543	0.488586	
Н		-2.446557	-1.808923	1.117603	
Н		-3.202606	-0.865705	0.191335	
O		2.102391	-1.454420	0.489265	
Н		2.797934	-1.203314	1.107646	
Н		2.347402	-2.341462	0.201886	
O		0.209930	2.547533	0.488683	
Н		0.842072	3.209108	0.184893	
Н		-0.343328	3.019131	1.121898	
Rotational symmetry=					3
Zero-point correction=					0.072644
Sum of electronic and zero-point Energies=				-254.321555	
Sum of electronic and thermal Energies=				-254.310582	
Sum of electronic and thermal Enthalpies=				-254.309638	
Sum of electronic and thermal Free Energies=					-254.363051

BaHCO₂⁺

Element Coordinates (Angstroms)					
X					
Ba			0.000000	-0.000000	
O		1.497801	-1.104647	0.000000	
O		1.497802	1.104647	0.000000	
C		2.111233	-0.000000	-0.000000	
Н		3.206701	-0.000001	-0.000002	
		symmetry nu			2
Zero-j	point	correction=			0.023022
Sum of electronic and zero-point Energies=					-214.529073
Sum of electronic and thermal Energies=					-214.524665
Sum of electronic and thermal Enthalpies=					-214.523721
Sum o	-214.557767				

BaHCO₃⁺

Element Coordinates (Angstroms)					
X	Y	Z			
Ba			-0.005978	-0.000001	
O		1.188757	-1.095252	0.000004	
O		1.135406	1.119154	0.000004	
C		1.779407	0.031705	0.000002	
O		3.090601	0.094193	-0.000005	
Н		3.449761	-0.800191	-0.000001	
Rotati	onal s	symmetry ni	 umber=		1
		correction=			0.028834
Sum of electronic and zero-point Energies=				-289.78504	
Sum of electronic and thermal Energies=				-289.77994	
Sum of electronic and thermal Enthalpies=				-289.77899	
Sum o	-289.81584				

$BaNO_2^+$

Element Coordinates (Angstroms)					
X	Y	Z			
Ba		0.723789	-0.000000	-0.000096	
N		-2.243898	0.000002	0.000358	
O		-1.551552	1.051823	0.000181	
O		-1.551559	-1.051822	0.000180	
Rotation	als	symmetry nu	mber=		2
Zero-po	int	correction=			0.009342
Sum of electronic and zero-point Energies=					-230.465677
Sum of electronic and thermal Energies=				-230.461078	
Sum of electronic and thermal Enthalpies=					-230.460133
Sum of electronic and thermal Free Energies=					-230.494952

BaNO₃⁺

Element Coordinates (Angstroms)					
X	Y	Z			
N			-1.906549		
O		-1.083483	-1.207823	0.000000	
O		1.083481	-1.207823	0.000000	
O		0.000000	-3.084568	0.000000	
Ba		0.000000	1.024063	0.000000	
		symmetry nu	umber=		2
Zero-p	oint	correction=			0.015811
Sum of electronic and zero-point Energies=					-305.667645
Sum of electronic and thermal Energies=					-305.662794
Sum of electronic and thermal Enthalpies=					-305.661850
Sum o	-305.697638				

BaOH⁺

Elemen	nt	Coordi	nates (Angs	troms)	
X	Y	Z			
Ba		0.003773	-0.309671	-0.000000	
O		0.003773	1.824496	0.000000	
Н		-0.241442	2.745579	0.000000	
Rotatio	nal s	symmetry nu	ımber=		1
Zero-po	oint	correction=			0.011228
Sum of electronic and zero-point Energies=					-101.175270
Sum of electronic and thermal Energies=				-101.171925	
Sum of electronic and thermal Enthalpies=				-101.170981	
Sum of electronic and thermal Free Energies=					-101.199396

${\bf CO_2}$

Element		Coordi	Coordinates (Angstroms)		
X	Y	Z			
				0.00000	
С		0.000000	0.000000	0.000000	
O		0.000000	0.000000	1.156497	
O		0.000000	0.000000	-1.156497	
Rota	tional s	symmetry nu	ımber=		2
Zero	-point	correction=			0.011877
Sum of electronic and zero-point Energies=					-188.586595
Sum of electronic and thermal Energies=				-188.583991	
Sum of electronic and thermal Enthalpies=					-188.583047
Sum of electronic and thermal Free Energies=					-188.607276

H_2CO_3

Element Coordinates (Angstroms)					
X	Y	Z			
O			-0.675457	-0.000020	
О		0.000007	1.298796	-0.000093	
C		-0.000000	0.098509	-0.000007	
O		1.083278	-0.675465	0.000116	
Н		1.843697	-0.087028	0.000121	
Н		-1.843698	-0.087013	-0.000108	
Rotatio	2				
Zero-point correction=					0.040335
Sum of electronic and zero-point Energies=					-264.99563
Sum of electronic and thermal Energies=					-264.99196
Sum of electronic and thermal Enthalpies=					-264.99101
Sum of	-265.02083				

H_2O

Element	Element Coordinates (Angstroms)					
X Y	Z					
O	0.000000	0.000000 0.116444				
Н	0.000000	0.760003 -0.465774				
Н	-0.000000	-0.760003 -0.465774				
Rotational	2					
Zero-point	0.021646					
Sum of elec	-76.418282					
Sum of elec	-76.415447					
Sum of elec	-76.414502					
Sum of elec	-76.435910					

H_3O^+

Element Coordinates (Angstroms)							
X	Y	Z					
O		0.000000	0.000000	0.073417			
Н		0.000000	0.936910	-0.195779			
Н		0.811388	-0.468455	-0.195779			
Н		-0.811388	-0.468455	-0.195779			
Rotational symmetry number=					3		
Zero-point correction=					0.034879		
Sum of electronic and zero-point Energies=					-76.682618		
Sum of electronic and thermal Energies=				-76.679713			
Sum of electronic and thermal Enthalpies=				-76.678768			
Sum of electronic and thermal Free Energies=					-76.700703		

$\mathrm{CH_3CO_2H}$

Element Coordinates (Angstroms)					
X		Z			
C			0.153620		
C		1.052240	-0.914069	0.000000	
O		0.197069	1.337514	0.000000	
Н		2.035505	-0.456382	0.000000	
Н					
Н		0.932535	-1.547175	-0.878222	
O		-1.241602	-0.369775	0.000000	
Н			0.371517		
Rotational symmetry number=					1
Zero-point correction=					0.062255
Sum of electronic and zero-point Energies=					-229.045439
Sum of electronic and thermal Energies=					-229.040873
Sum of electronic and thermal Enthalpies=					-229.039929
Sum of electronic and thermal Free Energies=					-229.072735

HF

Element	Element Coordinates (Angstroms)						
X Y	Z						
Н	0.000000	0.000000	-0.826602				
F	0.000000	0.000000	0.091845				
Rotational symmetry number= 1							
Zero-point correction=				0.009458			
Sum of electronic and zero-point Energies=				-100.451878			
Sum of electronic and thermal Energies=				-100.449518			
Sum of electronic and thermal Enthalpies=				-100.448574			
Sum of electronic and thermal Free Energies=				-100.468277			

HNO_2

Element							
X Y	Z						
O	-1.092843	-0.219826	-0.000001				
N	-0.165955	0.481674	0.000001				
Н	1.705046	0.427828	-0.000006				
O	1.024923	-0.255117	0.000001				
Rotational	1						
Zero-point	0.020791						
Sum of ele	-205.699832						
Sum of ele	-205.696644						
Sum of ele	-205.695700						
Sum of ele	-205.723778						

HNO₃

Element Coordinates (Angstroms)							
X Y	Z						
N	-0.143366	0.034666	0.000000				
O	1.112081	-0.554669	-0.000000				
O	O -0.156239 1.237185 -0.000000						
O	-1.044557	-0.738184	-0.000000				
Н	1.713288	0.202682	0.000000				
Rotational	1						
Zero-point	0.027109						
Sum of elec	-280.886260						
Sum of electronic and thermal Energies=				-280.882797			
Sum of elec	-280.881852						
Sum of electronic and thermal Free Energies= -280.91							

HCO_2H

Element Coordinates (Angstroms)					
X	Y	Z			
C			0.397580	0.000004	
O		1.128396	-0.263469	0.000005	
O		-1.110898	-0.089707	-0.000007	
Н		0.106733	1.493071	0.000016	
Н		-1.047668	-1.053142	-0.000016	
Rotational symmetry number=					1
Zero-point correction=					0.034175
Sum of electronic and zero-point Energies=					-189.745763
Sum of electronic and thermal Energies=					-189.742603
Sum of electronic and thermal Enthalpies=					-189.741659
Sum of	-189.769825				